MEASURING GALAXY CLUSTERING AND THE EVOLUTION OF [CII] MEAN INTENSITY WITH FAR-IR LINE INTENSITY MAPPING DURING $0.5 < z < 1.5$

B. D. Uzgil[1,2], J. E. Aguirre[1], and C. M. Bradford[2]
Draft version May 9, 2014

ABSTRACT

Infrared fine-structure emission lines from trace metals are powerful diagnostics of the interstellar medium in galaxies. We explore the possibility of studying the redshifted far-IR fine-structure line emission using the three-dimensional (3D) power spectra obtained with an imaging spectrometer. The intensity mapping approach measures the spatio-spectral fluctuations due to line emission from all galaxies, including those below the individual detection threshold. The technique provides 3D measurements of galaxy clustering and moments of the galaxy luminosity function. Furthermore, the linear portion of the power spectrum can be used to measure the total line emission intensity including all sources through cosmic time with redshift information naturally encoded. Total line emission, when ratioed to the total star formation activity and/or other line intensities reveals evolution of the interstellar conditions of galaxies in aggregate. As a case study, we consider measurement of [CII] autocorrelation in the $0.5 < z < 1.5$ epoch, where interloper lines are minimized, using far-IR/submm balloon-borne and future space-borne instruments. In this context, we compare the intensity mapping approach to blind galaxy surveys based on individual detections. We find that intensity mapping is nearly always the best way to obtain the total line emission because galaxy surveys lack either depth or sufficient volume to overcome cosmic variance. Even if absolute mean intensity is not desired, intensity mapping is often the most efficient way to measure the power spectrum shape, depending on the details of the luminosity function and the telescope aperture.

Keywords: far-infrared spectroscopy; galaxy redshift surveys

1. INTRODUCTION

Various observational techniques in astronomy, including, but not limited to, photometric and spectroscopic stacking analysis, $P(D)$ fluctuation analysis, and recently, cosmological spectral deconvolution (cf. Dole et al. (2006); Glenn et al. (2010); de Putter et al. (2014) for examples of each), have been developed to provide a means to study the nature of galaxies that are otherwise too faint to be detected individually at high significance. These methods rely heavily on interpreting the statistical and aggregate properties of the extragalactic sources, and yet the insight they have provided into the nature of galaxies and their evolution with cosmic time has been invaluable.

Line intensity mapping, or 3-D tomographic mapping, is another technique that allows astronomers to probe extragalactic light from all sources, including the faintest galaxies and even diffuse intergalactic emission. An intensity mapping survey of a spectral line at different frequencies produces a fully three dimensional data cube containing "tomographic scans" of the Universe along the spectral (i.e., redshift) direction. The spatial fluctuations in line emission, contained in the data cube, are then decomposed into the power spectrum. Atomic (Gong et al. 2012; Visbal et al. 2011) and molecular (Lidz et al. 2011; Gong et al. 2011) transitions – such as the 21-cm spin flip transition from H°, CO (2-1), and [CII] $158\mu m$ – have been investigated as candidates for intensity mapping experiments during the Epoch of Reionization (EoR). Of these, the neutral hydrogen case is

badeu@sas.upenn.edu
[1] University of Pennsylvania, Philadelphia, PA 19104
[2] Jet Propulsion Laboratory

undoubtedly the most developed in terms of its standing in the literature (cf. Morales & Wyithe (2010) for a review) and in the experimental arena (e.g., PAPER (Parsons et al. 2013), MWA (Tingay et al. 2013)) because intensity mapping is the only means of studying the intergalactic HI light. [CII] later emerged as an EoR intensity mapping candidate since it both offers a way to probe the clustering of sources from the faint-end of the luminosity function, and provides an opportunity for cross-correlation with the HI datasets (Gong et al. 2012).

Aside from tracing large-scale structure, [CII] also contains astrophysical information about the conditions in star-forming galaxies. With an ionization potential of 11.6 eV, it arises in both ionized and neutral atomic gas. Empirically, it is an important coolant, often the brightest single line in the spectrum of a star-forming galaxy, emitting as much as 0.5–1% of the total FIR luminosity (Malhotra et al. 1997; Luhman et al. 1998; Stacey et al. 2010; Graciá-Carpio et al. 2011). The ratio of the [CII] luminosity to the total bolometric luminosity can be used as a diagnostic tool that provides: (1) a measure of the star-formation activity, (2) a measure of the spatial extent (or "mode") of star formation, and (3) an AGN/starburst discriminant (Hailey-Dunsheath et al. 2010; Stacey et al. 2010; Graciá-Carpio et al. 2011; Sargsyan et al. 2012; Díaz-Santos et al. 2013).

The broader suite of far-IR lines probes all phases of the interstellar medium, and the negligible optical depth of galaxies at far-IR wavelengths ensures that even the most heavily embedded regions where stars form and black holes grow are revealed. For the atomic and ionized medium, the key far-infrared emission lines are those of C, N, & O (e.g., [OI]$63\mu m$, $146\mu m$, [CII]$158\mu m$,

[OIII]52μm, 88μm, [NIII]57μm, and [NII]122 μm, 205 μm). The emitting species cover more than an order of magnitude in ionization potential and they strongly constrain the density and temperature of the ionized and neutral gas, and the strength and hardness of the interstellar radiation field. These physical parameters then reveal the relative importance of the black hole vs. the hot young stars to the overall energy budget, and constrain the stellar effective temperatures (Rubin 1985; Dale et al. 2004; Colbert et al. 1999; Malhotra et al. 2001; Ferkinhoff et al. 2011; Lebouteiller et al. 2012, e.g.). The suite of carbon, oxygen and nitrogen transitions also measure abundances (Garnett et al. 2004; Lester et al. 1987; Nagao et al. 2011).

A power spectrum analysis of 3D tomography using the far-IR fine structure lines would expand upon recent works that utilize the fluctuations in emission rather than individual object detections to study the properties of dusty, star-forming galaxies (DSFGs) with continuum data. (See Casey et al. (2014) et al for a review of DSFGs at the redshifts of interest to this study.) These studies, using $P(D)$ (Glenn et al. 2010; Béthermin et al. 2011) or a 2-D power spectrum (Viero et al. 2012) analysis, have already shed light on some aspects (such as galaxy number counts or spatial clustering) of the bulk of these systems from $z = 1-3$, but they are limited by source confusion or uncertainties associated with the lack of redshift information, respectively. Redshift ambiguities can be removed to some extent with galaxy-by-galaxy surveys with the interferometers ALMA or NOEMA, or with an instrument like X-Spec, a proposed multi-object spectrometer for CCAT. However, the interferometer surveys will be expensive and will cover very little sky, and the CCAT surveys, though faster, will not reach the faintest galaxies in the luminosity function. Power spectrum treatment of the 3-D datasets naturally combines the redshift precision of spectral measurements, while including all sources in the luminosity function, and can be carried out with an instrument that does not require exquisite point-source sensitivity.

This sensitivity of the line intensity mapped power spectrum to galaxies below the individual detection threshold, indeed to the mean aggregate intensity in the line from all sources, is a unique line of inquiry for the galaxy populations. An example of using the power spectrum to determine luminosity density can be found in Planck Collaboration et al. (2013), although the results discussed there were derived from the 2-D angular power spectrum of IR continuum fluctuations, which relies on fits which include uncertainties in the dust spectral energy distributions, for instance. With inherent redshift information from the spectral line, such an observation of the 3-D power spectrum would ascertain the cosmic evolution of the Universe's total output in a given line with a level of precision not available by other means.

Line intensity mapping experiments targeting the fine structure metal lines at post-Reionization redshifts can offer a proof of principle of the approach, as in measurements of the HI autocorrelation power spectrum at $z \sim 0.8$ (Chang et al. 2010; Switzer et al. 2013). While not accessible from the ground, a balloon- or space-borne intensity mapping experiment with broad wavelength coverage could in principle measure the mean intensities of these lines through cosmic time, thereby charting the evolution of the star-formation conditions in galaxies in an absolute, aggregate sense. Here we consider a first step in this direction, a measurement of [CII] autocorrelation in multiple bins through the $0.5 < z < 1.5$ epoch. [CII] and far-IR lines in general ought to be particularly well-suited to this time frame, as $z \sim 1.5$ is believed to be the peak in the dust attenuation in galaxies, when roughly 80% of the cosmic star formation rate density is obscured and captured only in the infrared emission of re-processed starlight by dust grains (Burgarella et al. 2013). From a practical standpoint, [CII] in this epoch is relatively free of interloper lines, as we will see.

The organization of this paper is as follows. We have estimated the mean intensity for a suite of fine structure IR emission lines, including the [CII] line, based on the IR luminosity function and empirical line-to-IR luminosity correlations, and present these results in the context of a power spectrum model in Section 2. In Section 3, we envision suitable platforms for conducting the [CII] intensity mapping experiment and discuss the feasibility of detecting the [CII] power spectra in terms of the signal-to-noise ratio (SNR). From the power spectra, we provide estimates for accuracy on measuring the mean [CII] intensity as a function of redshift. To better assess the value of intensity mapping studies in the case of [CII] at moderate redshifts, and of intensity mapping experiments in general, we compare in Section 4 the performance of the intensity mapping approach against spectroscopic galaxy surveys that rely on individual detections of sources to measure the power spectrum. In particular, we examine the effects of variations in luminosity function shape, aperture diameter (and, consequently, voxel size), and experimental noise on the ability of each observational method to measure the power spectrum and provide a complete view of the galaxy population.

2. PREDICTIONS FOR FIR LINE POWER SPECTRA

2.1. *Relationship Between Galaxy Populations and Fluctuation Power*

The complete autocorrelation power spectrum of a given FIR line i as a function of wavenumber k, $P_{i,i}(k,z)$, can be separated into power from the clustering of galaxies, $P_{i,i}^{clust}(k,z)$ and a Poisson term arising from their discrete nature, $P_{i,i}^{shot}(z)$. We compute the full nonlinear matter power spectrum, $P_{\delta,\delta}(k,z)$, using the publicly available code HALOFIT+ (http://camb.info), which has been the standard tool for predicting matter power spectra upon its success in fitting state-of-the-art dark matter simulations over a decade ago (Smith et al. 2003). The clustering component of the line power spectrum is then written as

$$P_{i,i}^{clust}(k,z) = \bar{S}_i^2(z)\bar{b}_i^{\,2}(z)P_{\delta\delta}(k,z). \qquad (1)$$

Here we have implicitly assumed that the fluctuations in line emission trace the matter power spectrum with some average bias, $\bar{b}_i(z)$. For our target redshift range, $\bar{b}_i$ is reasonably well-constrained to be between 2 and 3.(Cooray et al. 2010; Jullo et al. 2012), so we have assumed a single bias at each redshift, although a more sophisticated model would allow for a variation of the source bias with the host halo mass (and, subsequently, luminosity).

The mean line intensity, $\bar{S}_i(z)$, in units of Jy sr^{-1}, can be calculated as

$$\bar{S}_i(z) = \int \mathrm{d}n_i \frac{L_i}{4\pi D_L^2} y_i D_A^2, \qquad (2)$$

where the integration is taken with respect to n_i, the number of galactic line emitters per cosmological comoving volume element. The factor y_i is the derivative of the comoving radial distance with respect to the observed frequency, i.e. $y = d\chi/d\nu = \lambda_{i,rest}(1+z)^2/H(z)$, and D_A is the comoving angular distance.

Finally, the shot noise component of the total line power spectrum—with the same units as the clustering term, namely, Jy^2 sr^{-2} (Mpc h^{-1})^3—takes the form

$$P_{i,i}^{shot}(z) = \int \mathrm{d}n_i \left(\frac{L_i}{4\pi D_L^2}\right)^2 \left(y_i D_A^2\right)^2. \qquad (3)$$

2.2. Calculating IR line volume emissivity

The number density of line emitters and the line luminosity that appear in equations (2) and (3) can be derived by a variety of methods. In earlier papers on intensity mapping of molecular and fine-structure emission lines at high redshift ($z \gtrsim 6$), one approach involved using the dark matter halo mass function in lieu of the line emitter density (and invoking a one-to-one correlation between halos and galaxies, which is reasonable at high redshifts). The line luminosity, in turn, could be scaled according to the star formation rate, which was related to halo mass via a proportionality constant comprised of factors describing the fraction of baryons available for star formation, as well as the dynamical timescale for star formation and a duty cycle for emission. While this approach is perhaps justified for the very early Universe (given the lack of information about the galaxy luminosity function at high redshift), the situation at later times is better understood; we make use of empirical constraints on the $z \sim 1$ epoch from FIR/submm number counts and observations of FIR line emission in galaxies.

We first employ the empirically-constrained, backwards-evolution model of the IR luminosity function $\Phi(L_{IR}, z)$ from Béthermin et al. (2011) (hereafter B11) to predict the number of galaxies with luminosity L_{IR} at a given redshift in some comoving volume of the Universe per logarithmic luminosity interval, i.e., $\frac{\mathrm{d}N(L_{IR},z)}{\mathrm{d}V \mathrm{dlog}_{10} L_{IR}}$ or $\frac{\mathrm{d}n_{IR}}{\mathrm{dlog}_{10} L_{IR}}$.

To convert the infrared luminosity to a line luminosity, we apply the relation for L_i as a function of L_{IR} provided by Spinoglio et al. (2012). The fit in their paper was based on the collection of ISO-LWS observations of local galaxies in Brauher et al. (2008). For example, we reproduce below the relation for [CII]:

$$\log_{10} L_{[\mathrm{CII}]} = (0.89 \pm 0.03)\log_{10} L_{IR} - (2.44 \pm 0.07), \quad (4)$$

indicating that [CII] is suppressed for higher luminosity systems. The choice of using local L_i-L_{IR} relations for our study of $z \sim 1$ emitters may be unrealistic due to findings that suggest the so-called "deficit" in [CII] and other FIR lines evolves with redshift such that the high-z counterparts to local systems do not exhibit suppressed FIR line emission. The local IR relations then can be interpreted as underestimating emission of the fine structure lines, since we likely overestimate the deficiency in the higher redshift, high luminosity systems of our model. While in Section 4 we explore variations in the shape of the IR luminosity function and consider an alternative line-to-IR luminosity ratio, we use the combined Bethermin-Spinoglio model to predict line intensities and adopt it as our fiducial model throughout this paper.

Next, it becomes possible to write the cosmic mean intensity and shot noise of the line, in units of Jy sr^{-1}, as a function of redshift based on the B11 luminosity function and Spinoglio et al. (2012) $L_i - L_{IR}$ relation as

$$\bar{S}_\mathrm{i}(z) = \int_{L_{IR,min}}^{L_{IR,max}} \mathrm{dlog} L_{IR} \Phi(L_{IR}, z) \frac{f_i L_{IR}}{4\pi D_L^2} y D_A^2 \quad (5)$$

$$P_{i,i}^{shot}(z) = \int_{L_{IR,min}}^{L_{IR,max}} \mathrm{dlog} L_{IR} \Phi(L_{IR}, z) \left(\frac{f_i L_{IR}}{4\pi D_L^2} y D_A^2\right)^2 \quad (6)$$

where f_i, i.e. $\frac{L_i(L_{IR})}{L_{IR}}$, is the fraction of IR luminosity emitted in line i, as computed from equation (3). In other words, we have written $\bar{S}_i$ and $P_{i,i}^{shot}(z)$ as the first and the second moments of the luminosity function.
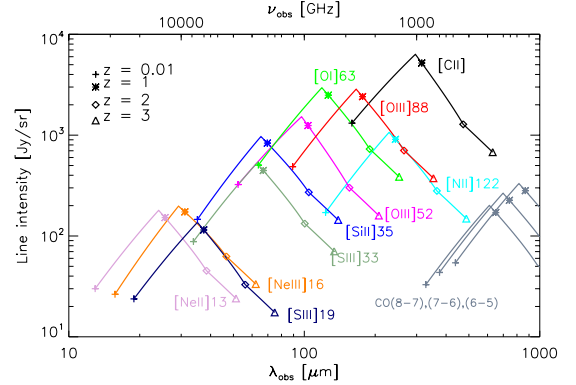

Figure 1. : Intensity of fine structure line emission as a function of observed wavelength for the empirical model based on the B11 luminosity function. Intensities of CO lines, which are not included in the IR luminosity relations from Spinoglio et al. (2012), have been estimated using a luminosity scaling provided by Carilli (2011).

The resulting mean intensities for a variety of FIR lines are plotted in Figure 1 as a function of redshift and observed wavelength. $\bar{S}_i$ vs λ_{obs} can be interpreted as identifying the dominant source of fluctuations, according to our model, for a given frequency. As a specific example, if the target line of an observation is [OI]63μm at $z = 1$, it is necessary to distinguish between the target line and interlopers like [OIII]88μm from $z = 0.4$ and [OIII]52μm from $z = 1.4$, which contribute power at the observed frequency. Visbal & Loeb (2010) showed how the cross spectra can be used to differentiate between a target line and a contaminating line (or "bad line", in their words), since emitters at different redshifts will be spatially uncorrelated. For the observed wavelengths of

[CII], however, it is apparent from Figure 2 that, with the exception of contributions from [OIII]88μm and CO(8-7) near [CII] at $z \sim 0.01$ and $z > 2$, respectively, the [CII] line is relatively unaffected by interloper lines—a result of its luminosity and spectral isolation. It is for this practical reason, and for the astrophysical significance of [CII] mentioned in the Introduction, that we focus the remainder of this paper largely on [CII] emission.

2.3. *[CII] Luminosity Functions and Expected Power Spectra*

As laid out in Equation 1, $P^{clust}_{[CII],[CII]}$ is sensitive to intensity fluctuations from the full range of normal ($L_{IR} < 10^{11}$ L$_\odot$) to ULIRG-class ($L_{IR} > 10^{12}$ L$_\odot$) systems because its amplitude is proportional to the mean line intensity, squared. The information contained in a power spectrum of individually detected galaxies is, in contrast to the line intensity mapping approach, necessarily limited to galaxies which are above a certain detection threshold, or $L_{IR,min}$. Figure 2 shows the integrated luminosity functions for [CII] in our model, which gives a sense of the depth that a galaxy survey must reach in order to completely probe the full integrated [CII] emission, i.e. all of $\bar{S}_i$. In this section, we examine the role of the various luminosity ranges on the amplitude of the observed [CII] power.

Power spectra at four representative redshifts ($z = 0.63, 0.88, 1.16,$ and 1.48) comprised of the sources above a few different survey depths, or $L_{IR,min}$, are represented by Figure 3. (Note that we use $\Delta^2_{[CII],[CII]} = k^3 P_{[CII], [CII]}(k)/(2\pi^2)$ when plotting the power spectrum. In this notation, the factor k^3 cancels out the volumetric units of $P_{\delta,\delta}(k,z)$ and the integral of $\Delta^2_{[CII],[CII]}$ over logarithmic k bins is equal to the variance in real space.) At these redshifts, respectively, the average linear bias has been assumed to be $\bar{b} = 2.0, 2.3, 2.6,$ and 2.9. In this Figure, we see the clustering amplitude decrease as the IR detection threshold is raised from 10^8 L$_\odot$ to 10^{12} L$_\odot$. (Note that the reduction in the clustering amplitude is precisely the square of the factor of reduction in $\bar{S}_{[CII]}$ plotted in Figure 2.) The level of decrease in clustering power as a result of raising $L_{IR,min}$ is most dramatic at the lower end of the redshift range of interest, when the luminosity function is represented mostly by normal galaxies and LIRGs. As ULIRGs rise to dominate the IR luminosity function at $z \sim 1.5$, the amplitude of the clustering component of $P_{[CII],[CII]}(k,z)$ becomes relatively robust up to $L_{IR,min} \sim 10^{11}$ L$_\odot$, implying that a large fraction of the fluctuations are captured at this depth; we infer from Figure 2 that, at $z = 1.48$, individually resolving galaxies at a depth of 6×10^{11} will recover half of the [CII] light, at which point the remaining power of unresolved fluctuations is 25% according to our model. For redshifts $z = 0.63, 1.16$ and 3.0, the corresponding depths to observe half-light are $\sim 10^{11}$, 2×10^{11}, and 10^{12} L$_\odot$, respectively.

3. THE [CII] POWER SPECTRUM

3.1. *Observational Sensitivity to the Power Spectrum*

We present in this section an assessment of detectability of the [CII] power spectrum. In order to quantify the
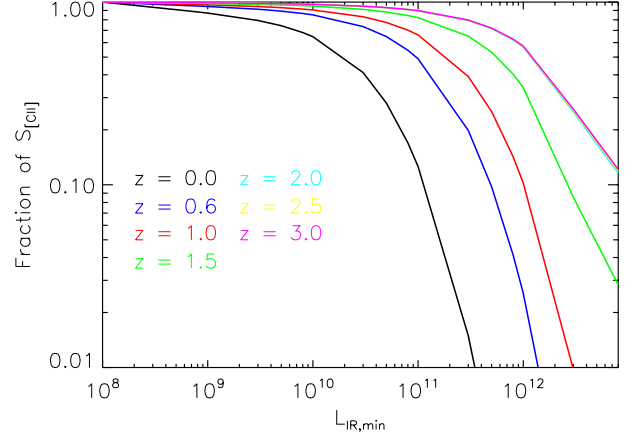

Figure 2. : The fraction of total [CII] mean intensity as a function of lower limit in the luminosity function. Different color curves represent different redshifts, as labeled on the plot.
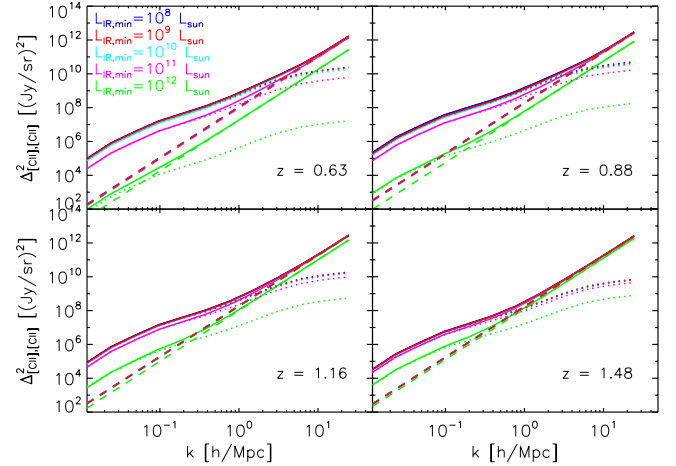

Figure 3. : Predicted [CII] autocorrelation power spectra from $z = 0.63$ to $z = 1.48$. Blue, red, cyan, magenta, and green curves represent the power spectrum computed with a lower limit in the luminosity function corresponding to 10^8, 10^9, 10^{10}, 10^{11}, and 10^{12} L$_\odot$, respectively.

observational sensitivity, we adopt a realistic experimental platform with uninterrupted wavelength coverage in the redshift range of interest, namely, from 240 to 420 μm. This range is further divided into four bands to enable measuring redshift evolution in the signal. The width of each band has been set to span a redshift range of $\frac{\Delta z}{z_{center}} = 0.25$ to ensure there is no significant cosmological evolution within the band. Fiducial experimental parameters are summarized in Table 1. The telescope aperture diameter, D_{ap}, and survey area, A_{survey}, are taken as 2.5 m and 1 deg^2, respectively, though we explore the effect of varying D_{ap} and A_{survey} on the Signal-to-Noise Ratio (SNR) (cf. Figure 5).

To define the survey depth, we adopt the quantity

$$f_{err} \equiv \frac{\sigma_N}{\sqrt{t^{vox}_{obs}} \bar{S}_i} \qquad (7)$$

which we call the fractional error. It is simply the inverse of the SNR on the mean intensity in a single voxel. Here σ_N^2 is the instrument sensitivity (noise equivalent intensity, or NEI, in units of Jy sr^{-1} s$^{1/2}$, $\bar{S}_i$ is the mean intensity and t_{obs}^{vox} is the observing time per voxel. Error bar estimates and the total SNR for the power spectrum are calculated by assuming a spectrally flat noise power spectrum, so that the noise power in each voxel, P_N, is written as

$$P_N = \sigma_N^2 \frac{V_{vox}}{t_{obs}^{vox}} \qquad (8)$$
$$= \left(f_{err}\bar{S}_i\right)^2 V_{vox}$$

where σ_N^2 is the instrument sensitivity (noise equivalent intensity, or NEI, in units of Jy sr^{-1} s$^{1/2}$, V_{vox} is the volume of a voxel, and t_{obs}^{vox} is the time spent observing on a single voxel. The variance of a measured k, $\sigma^2(k)$, is then written as

$$\sigma^2(k) = \frac{(P_{i,i}(k) + P_N(k))^2}{N_{modes}}, \qquad (9)$$

where N_{modes} is the number of wavemodes that are sampled for a given k bin of some finite width $\Delta\log(k)$. (We have chosen $\Delta\log(k) = 0.3$ for this analysis.)

The total SNR, in turn, is calculated from the expression

$$SNR_{tot} = \sqrt{\sum_{bins} \left(\frac{P_{i,i}(k)}{\sigma(k)}\right)^2} \qquad (10)$$

The expected [CII] power spectrum, with corresponding predictions for SNR, at the same redshifts from Figure 3 are shown in Figure 4. In calculating the power spectrum sensitivity for these power spectra, the two lowest line-of-sight modes and the lowest transverse mode are not included, since these modes will likely be compromised by the necessity of continuum foreground subtraction and beam-differencing in the fluctuation analysis. (The exact effect of continuum subtraction will need to be modeled via simulation.)

Table 1 shows our instrument concepts. We specify a 25-beam grating spectrometer covering the 240-420 μm band, each with 64 $R = 450$ spectral channels operating near the photon background limit, illuminated with a 2.5-meter telescope. We consider a balloon experiment for which the photon background is due to 1% emissivity in the atmosphere (a conservative average value) and 4% in the telescope. A 200 hour integration (as might be obtained in a long duration balloon flight) over the 1 square degree with this system results in the σ_N, f_{err}, and line sensitivity values tabulated. We also consider a similar instrument on a cryogenic space-borne platform. The sensitivity in this case is obtained by specifying a detector sensitivity which adds $\sqrt{2}$ in quadrature to the noise in the photon background from the combination of zodiacal light, galactic dust, and a 6-K telescope with 4% emissivity, similar to the proposed BLISS instrument for SPICA (e.g., see **?** (SPIE on BLISS)). As the tabulated depths indicate, the space-born system is much

more sensitive. Nevertheless, the balloon-borne experiment is capable of measuring the power spectrum with good sensitivity, and all error bars in plotted power spectra in this paper are based on the 200-hour balloon experiment.

We find that the total power spectrum, including power from both shot noise and clustering, is observable with SNR> 10 in the redshift range from $z = 0.88 - 1.48$; the clustering power, in turn, can be detected with SNR > 5 at all examined redshifts.

In Figure 5 we examine the effect on SNR of changing the survey area and telescope aperture, where the SNR has been plotted as a function of k. To better demonstrate how the observational parameters drive the behavior of SNR(k) illustrated in this Figure, we rewrite P_N in terms of the parameters from Table 1, giving

$$P_N = \left(\sigma_N^2 A_{pix}\Delta r_{los}^{vox}\right) / \left(\frac{t_{survey}}{n_{beams}/N_{instr}^{spatial}}\right)$$
$$= \left(\sigma_N^2 A_{pix}\Delta r_{los}^{vox}\right) / \left(\frac{t_{survey}N_{instr}^{spatial}}{A_{survey}/A_{pix}}\right) \qquad (11)$$
$$= \sigma_N^2 \frac{\Delta r_{los}^{vox} A_{survey}}{t_{survey}N_{instr}^{spatial}}$$

In this form, it becomes apparent that—with fixed number of spatial pixels, spectral resolution, and total observing time—the only factor driving up the amplitude of noise power is the survey area; the effect of increasing aperture only allows access to higher wavenumbers, which is important for subtracting the shot noise from the total power to reveal the clustering.

3.2. Measuring $\bar{S}_{[CII]}(z)$

As noted above, intensity mapping is naturally sensitive to the full range of galaxy luminosities through
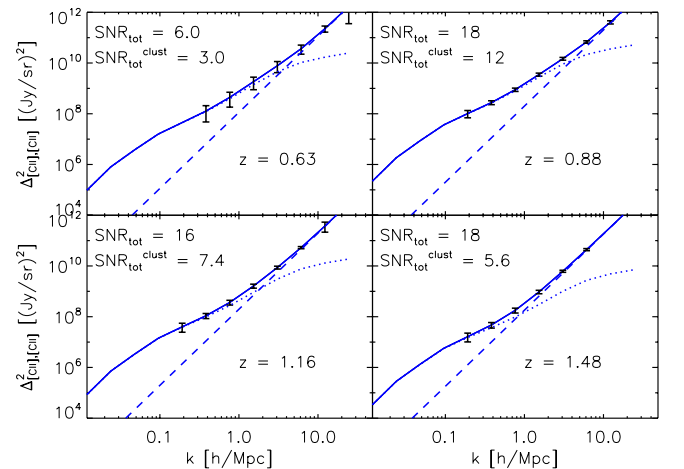

Figure 4. : Predicted [CII] power spectra with error bar estimates from $z = 0.63$ to $z = 1.48$ for telescope with 2.5 meter aperture and a survey area of 1 square degree, and with a total observing time of 200 hours. Dotted curves indicate power from clustering (including contributions from linear and nonlinear terms), and dashed curves indicate the contribution from shot noise power.

Table 1: Parameters for Envisioned Experimental Platforms

A_{survey} (deg^2)			1.0	
D_{ap} (m)			2.5	
$R = \lambda_{obs}/\Delta\lambda$			450	
N of Spectral Channels			64	
N of Spectrometers (instantaneous spatial pixels)			25	
t_{obs}^{survey} (hr)			200	

z_{cen} for [CII]	0.63	0.88	1.16	1.48
V_{voxel} (Mpc^3 h^{-3})	0.36	0.81	1.59	2.87
$\bar{S}_{\rm [CII]}$ (Jy sr^{-1})	4.56×10^3	6.33×10^3	4.05×10^3	2.55×10^3

Experimental Platform	Atmospheric Balloon				Cryogenic Satellite			
σ_N (10^7 Jy sr^{-1} sec$^{1/2}$)	3.4	2.1	1.5	1.0	0.030	0.034	0.039	0.043
Line Sensitivity, S_γ (10^{-18} W m^{-2} sec$^{1/2}$)	15.8	11.3	9.20	7.10	0.139	0.185	0.240	0.306
f_{err}	230	90.4	88	81	2.1	1.5	2.3	3.5

the mean intensity, which is imprinted in the linear (2-halo) clustering term. Shot noise must be accurately subtracted, and this should be straightforward given the high SNR in the shot-noise dominated k bins (Figure 5).Next, per Equation 1, it is necessary to divide out $P_{\delta,\delta}(k,z)$ and $\bar{b}_{\rm [CII]}^2(z)$.The confidence with which are *a priori* known quantities becomes lower as k increases. For example, the 1-halo power spectrum for DSFGs appears to be dependent on the IR luminosity of the contributing sources (Viero et al. 2012), indicating the need to map sufficiently wide areas that access k modes where the power is largely independent of the level of 1-halo power.

Returning to Figure 5, we see that, for the purpose of measuring $\bar{S}_{\rm [CII]}$ with the fiducial survey of 1 deg^2, there are two k bins ($k = 0.16$ and 0.27 h/Mpc) in which the 2-halo clustering accounts for at least 75% of the total power. (Surveys with $A_{survey} = 5.3$ and 10 deg^2, also shown in Figure 5, are wide enough to have three k bins available in the linear regime, but the sensitivity on the additional mode with $t_{obs}^{survey}= 200$ hours is marginal.) Thus, in considering the case of $A_{survey} = 1.0$ deg^2,
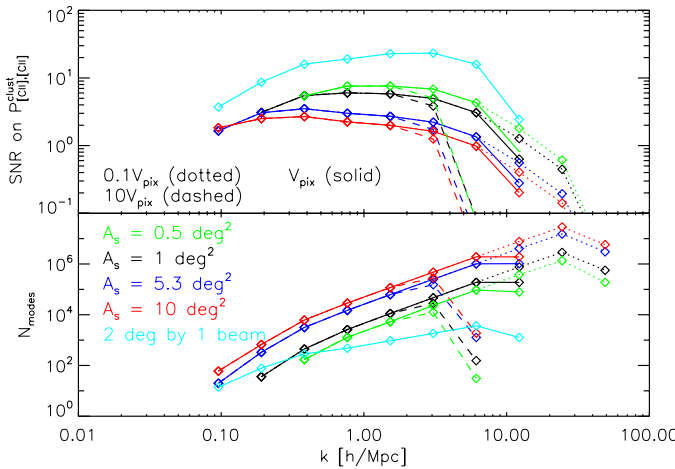
we find that it is possible to measure $\rho_{\rm [CII]}(z)$ within $\sim 10\%$ accuracy from $z = 0.63$ to $z = 1.48$, as shown in Figure 6, where the fractional uncertainty on $\bar{S}_{\rm [CII]}(k,z)$ has been calculated as half the fractional uncertainty on $P_{\rm [CII],[CII]}(k,z)$. In Figure 6, we also include, for comparison, an estimate for $\rho_{\rm [CII]}(z)$ based on the analytic fit to SFRD(z) provided by Hopkins & Beacom (2006) and flat ratios of $L_{\rm [CII]}/L_{IR} = 0.001$ and 0.003. (We use the standard relation between SFRD and infrared luminosity described in Kennicutt (1998).)
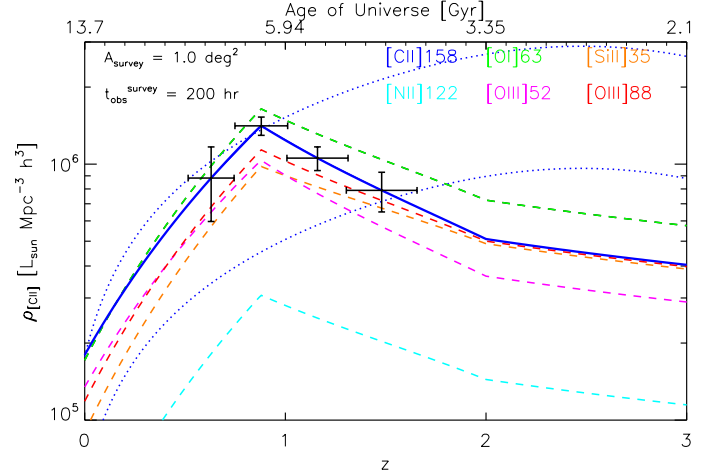

Figure 6. : Error bar estimates on $\rho_{\rm [CII]}$, as measured by the fiducial experiment, at observed redshifts $z = 0.63$, 0.88, 1.16, and 1.48. Errors in z correspond to the redshift space spanned by the spectrometer bandwidth. The solid blue curve is the underlying model for [CII] luminosity density. The luminosity density of other bright IR lines are shown as the dashed colored curves, and the dotted curve is an estimate for $\rho_{\rm [CII]}$ based on the fit to SFRD(z) provided by Hopkins & Beacom (2006), where we have used constant ratios of $L_{\rm [CII]}$ to L_{IR} equal to 0.001 (bottom curve) 0.003 (top curve) to convert from IR luminosity density to [CII] luminosity density.

Figure 5. : Signal-to-noise on the clustering term of the [CII] power spectrum $P_{\rm [CII], [CII]}^{clust}$ and number of modes as a function of k at $z = 0.88$. The black, blue, and red lines correspond to survey areas of 1.0, 5.3, and 10.0 deg^2, respectively. Telescopes with apertures yielding 0.1, 1, and 10 times the fiducial pixel volume, V_{vox}, are shown as the dotted, solid, and dashed lines, respectively.

4. OBSERVATIONAL STRATEGY: COMPARING INTENSITY MAPPING WITH TRADITIONAL GALAXY SURVEYS

Now let us turn to a question regarding the motivation for intensity mapping in general, as well as in the specific case of [CII] at the redshifts relevant to this study.
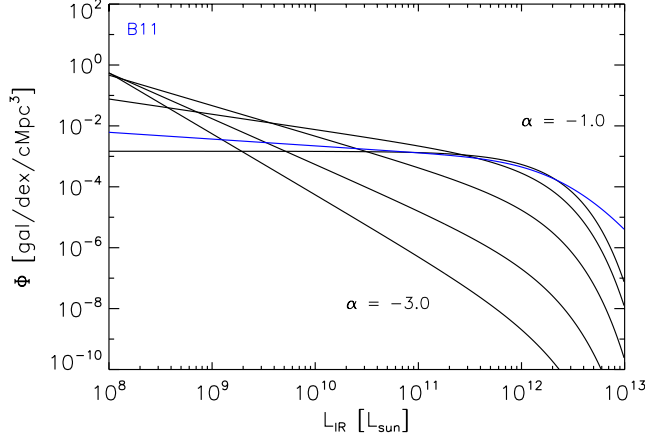
Figure 7. : Toy model IR luminosity functions with faint-end slope (from top to bottom) $\alpha = -1.0, -1.5, -2.0, -2.5, -3.0$. The B11 model (blue curve) is plotted for comparison.

Having identified the galaxy redshift surveys as an alternative method to measure the mean intensity of the line-emitting galaxy population and to measure the 3D clustering power spectrum, it is natural to draw a comparison of the two approaches.

The principal advantage of intensity mapping is that it naturally measures the mean intensity per equation 5, regardless of the shape of the luminosity function. Galaxy surveys always miss some of the light in the faintest galaxies, and this completeness problem is illustrated in Figure 9. To make concrete comparisons in what follows we employ toy models for the infrared luminosity function (Figure 7) written in the Schechter formalism—parametrized by the usual α, L_*, and ϕ_*—and normalize the total IR luminosity density according to B11 (cf. Appendix for details). We stress that these Schechter models are not intended to represent a real interpretation of the distribution of galaxies, but are merely helpful for illustrating the effect of the LF *shape* on the relative usefulness of intensity mapping and traditional galaxy surveys. In converting the IR LF to a line luminosity function, we use, in addition to the Spinoglio et al. (2012) relation for $L_{[CII]}/L_{IR}$, a conservative and flat line-to-IR luminosity ratio of 10^{-3}, relegating the luminosity-dependence of this ratio (and any redshift evolution) as a second order effect.

The line sensitivity, S_γ (units of W m^{-2} s$^{1/2}$), is the figure of merit for detecting an unresolved line in a point source, and we define individual detections at the 5σ level as having a flux above the instrumental noise in a voxel, i.e., above $5 \times S_\gamma t_{vox}^{-1/2}$. (For this analysis, we have assumed the galaxy surveys have reliable spectroscopic redshifts and thus neglect the problem of confusion noise.) A convenient expression, which explicitly ties the minimum detectable line luminosity to a set of theoretical and experimental parameters, for the detection threshold can be written as

$$L_{i,min} = 5 \times f_{err}\rho_i V_{vox}, \qquad (12)$$

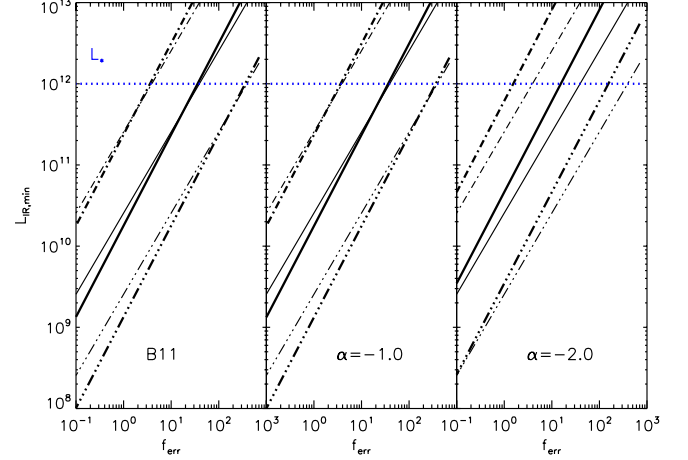Here, f_{err} is the fractional error (Eq. 7) and ρ_i is

Figure 8. : IR depth as a function the fractional error. Results are plotted for the B11 (leftmost panel) model as well as the toy Schechter functions (remaining panels). Solid curves correspond to the fiducial aperture, $d_{ap} = 2.5$ m. Dashed curves correspond to apertures scaled by a factor $\sqrt{\epsilon}$, where $\epsilon = 10$ (triple-dot-dashed) and $\epsilon = 0.1$ (dot-dashed). Thick curves correspond to our fiducial model for [CII] line intensity, based on Spinoglio fits, whereas thin curves denote the use of a constant ratio of $\frac{L_{[CII]}}{L_{IR}} = 10^{-3}$.

the comoving luminosity density of line i at some z, or $L_*\phi_*\Gamma(2 + \alpha, L/L_*)$ in the Schechter notation, so that equality holds between Equation 12 and the more conventional expression for the 5σ detection threshold:

$$\frac{L_{i,min}}{4\pi D_L^2} \Leftrightarrow 5 \times S_\gamma t_{vox}^{-1/2} \qquad (13)$$

The survey depths $L_{IR,min}$ as a function of f_{err}, V_{vox}, and α are plotted in Figure 8. Note that we are investigating the effect of changing telescope aperture, which only changes the transverse dimensions of V_{vox}.

Since the intensity mapping technique contains information in the power spectrum from sources below a given S_γ, we expect that regimes in which the majority of galaxies are too faint to be resolved are better-suited for intensity mapping observations than observations via the traditional galaxy survey. Inspection of Equation 12 yields that this scenario occurs for large voxels (or large beam sizes), large fractional errors, or steep luminosity functions where the bulk of the galaxy number density is comprised of galaxies with sub-L_* luminosities. These three limiting cases for the fiducial square degree survey at $z = 1.48$ are illustrated in Figures 9 and 10 for the experimental goals of measuring mean intensity and the clustering power spectrum, respectively.

As an example of the problem posed by steep luminosity functions for galaxy surveys aiming to measure the mean intensity, we find that for LFs with α of -1.5 (not shown) or -2.0, the galaxy surveys detect only 40% and 3% of the total [CII] light in integrating to an f_{err} of 10. Increasing the telescope aperture by a factor of $\sqrt{10}$ (shown as the triple-dot-dashed curves) boosts this fraction to 60% in the case of $\alpha = -1.5$, but still recovers 10% or less of the $\rho_{[CII]}$ for $\alpha = -2.0$. Note that an f_{err}
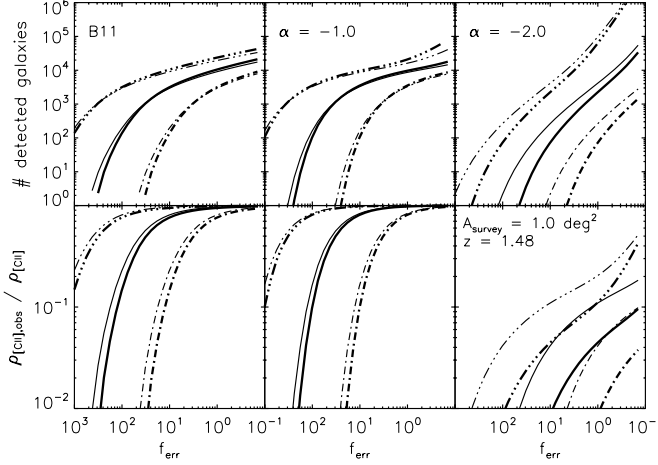
Figure 9. : The predicted number of [CII]-detected galaxies and observed fraction of [CII] luminosity density as a function of survey time for the square degree field. Results are plotted for the B11 (leftmost panel) model as well as the toy Schechter functions (remaining panels). Solid curves correspond to the fiducial aperture, $d_{ap} = 2.5$ m. Dashed curves correspond to apertures scaled by a factor $\sqrt{\epsilon}$, where $\epsilon = 10$ (triple-dot-dashed) and $\epsilon = 0.1$ (dot-dashed). Thick curves correspond to our fiducial model for [CII] line intensity, based on Spinoglio fits, whereas thin curves denote the use of a constant ratio of $\frac{L_{\rm [CII]}}{L_{IR}} = 10^{-3}$.

of 10 allows the galaxy survey to recover nearly 80% of the total [CII] light at $z = 1.5$ if $\alpha = -1.0$, but such a low fractional error requires either very low instrument noise or very long integration times—roughly 10^4 hours for the fiducial instrument when observing a square degree field, for instance. (We refer the reader to Table 2 for the conversions between f_{err} and integration time per voxel for the fiducial balloon experiment, as well as for the cryogenic satellite experiment.) Note that the integration time could be reduced by utilizing smaller survey fields like ultradeep pencil beams, but these surveys would be dominated by cosmic variance and characterization of the cosmic mean intensity, or, equivalently, the luminosity function, would be limited.

The top row Figure 9 breaks down the total emission in terms of the number of detectable galaxies. As is clear from comparison of panels in the top and bottom rows, a large sample of galaxies (of order 1,000 or greater) does not necessarily ensure an unbiased measure of the mean [CII] intensity. If, however, one extracts the aggregate, unresolved emission from [CII] via the intensity mapped power spectrum, one is essentially measuring $\frac{\rho_{[CII],obs}}{\rho_{[CII]}} = 1$ as soon as SNR on the linear clustering term of the power spectrum is sufficiently high, which was depicted in Figure 6.

There may be applications—such as measuring the BAO peak or searching for primordial non-Gaussianity in large-scale structure—for which the mean intensity is not required, and the shape of the power spectrum, rather than its absolute value, is of interest. For this application, we compare the SNR on a linear-term k bin (up to $k < 0.3$ h/Mpc) for both galaxy detection and

intensity mapping surveys (denoted, respectively, by the subscripts "GS" and "IM"), with the expressions:

$$\text{SNR}_{GS} = \frac{\sqrt{N_{modes}}}{1 + 1/(b_i^2 P_{\delta,\delta} \bar{n}_{gal})} \qquad (14)$$

$$\text{SNR}_{IM} = \frac{\sqrt{N_{modes}}}{1 + P_N/\left(\bar{S}_i^2 b_i^2 P_{\delta,\delta}\right)} \qquad (15)$$

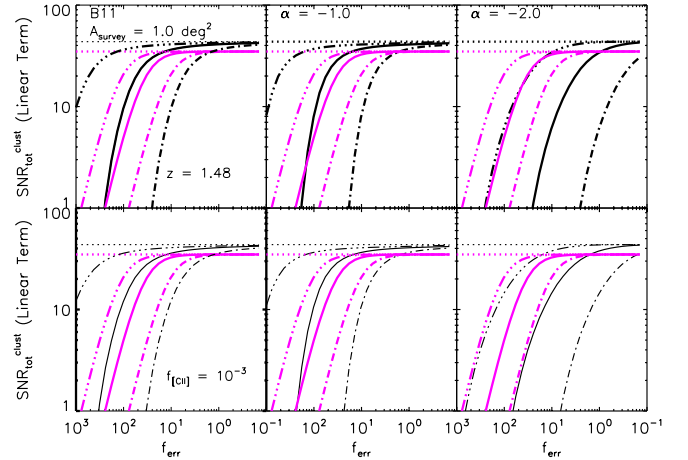$$= \frac{\sqrt{N_{modes}}}{1 + (f_{err}^2 V_{vox})/(b_i^2 P_{\delta,\delta})}$$

Figure 10. : Total Signal-to-Noise ratio on the linear portion of the clustering power spectrum of [CII] at $z = 1.48$ as a function of the fractional error. Results are plotted for the B11 (left panels) model as well as the toy Schechter functions (middle and right panels). SNR_{IM} and SNR_{GS} are plotted as the magenta and black curves, respectively. Solid curves correspond to the fiducial aperture, $d_{ap} = 2.5$ m. Dashed curves correspond to apertures scaled by a factor $\sqrt{\epsilon}$, where $\epsilon = 10$ (triple-dot-dashed) and $\epsilon = 0.1$. The horizontal dotted line is the maximum SNR possible for each approach as set by the number of modes in the survey volume, which is lower for the intensity mapping experiment due to our described mode removal. Results are shown for predictions of [CII] intensity based on the Spinoglio fits (top panel) and a constant ratio of $\frac{L_{\rm [CII]}}{L_{IR}} = 10^{-3}$ (bottom panel).

Even in this limited comparison of relative SNRs, the intensity mapping often outperforms galaxy surveys, as shown in Figure 10. For the steepest faint-end slope ($\alpha = -2.0$) we have tested, $\text{SNR}_{IM} > \text{SNR}_{GS}$ for all f_{err} and beam sizes (i.e., telescope apertures). For the flatter LFs, there are ranges of f_{err} where $\text{SNR}_{IM} > \text{SNR}_{GS}$ for the fiducial case, corresponding to when the galaxy surveys are shot-noise dominated. Figure 11 summarizes the results in Figure 10. It is important to remember that while surveys may detect a large number of galaxies, and thus attain appreciable SNR_{GS} on the power spectrum, the sample of detected galaxies may not yield a measurement of mean intensity, for which a large fraction of the total [CII] light must be observed (cf. Figure 9.)

In considering only the SNR on the linear clustering

Table 2: Conversions between t_{obs}^{vox} and f_{err} at $z = 1.48$

$t_{obs}^{vox} f_{err}^2$ ($\times 10^6$)	B11	$\alpha = -1.0$	$\alpha = -1.5$	$\alpha = -2.0$
Atmospheric Balloon	1.5378700	1.5667517	9.0373812	2.8255556
Cryogenic Satellite	0.028645231	0.029183196	0.016833533	0.0052630385
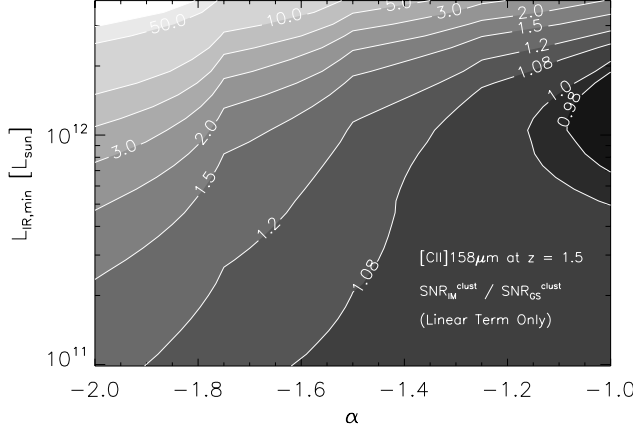
Figure 11. : Contours of $\mathrm{SNR}_{IM}/\mathrm{SNR}_{GS}$ for the linear term in the [CII] clustering power spectrum at $z = 1.5$, determined for a given depth (in L_{IR}) and IR LF faint-end slope α.

term ($k < 0.3$ h/Mpc) in our comparison, we do not address the potential of the 3D clustering power spectra to be used in the context of models which connect the host dark matter halos with their constituent galaxies by fitting to the observed 1-halo power. Since the 1-halo amplitude is highly sensitive to the luminosity of the contributing galaxy populations, we merely note in passing the potential of intensity mapping to constrain the distribution and types of galaxies within dark matter halos.

5. SUMMARY AND OUTLOOK

We have demonstrated the utility of the intensity mapping technique in measuring 3D power spectrum of bright FIR line emission at moderate redshifts, focusing on the important star-formation indicator [CII]. Fluctuations of FIR fine structure line intensities have been modeled by combining with the theorized dark matter power spectrum the empirically-constrained estimates of the IR luminosity from the B11 IR luminosity function and Spinoglio et al. (2012) line-to-L_{IR} relations. We have presented predictions for the measurement of the [CII] power spectrum between $0.63 < z < 1.48$, and found the power spectrum to be detectable in both clustering and shot noise terms in this redshift range with a modest experimental platform. On large scales, the fact that the clustering amplitude of [CII] fluctuations is proportional to the mean [CII] intensity indicates the potential for measuring cosmic evolution of aggregate [CII], or of any target line, emission with the line intensity mapping approach. For the fiducial experiment considered in this paper, we have found that it would be possible to measure the [CII] luminosity density with fractional errors on the order of 10%. In examining the effect of luminosity function shape, telescope aperture, and fractional error (or instrument noise level) on the relative performances of intensity mapping to galaxy surveys, we have further demonstrated that, in the case where experiments with low fractional errors are not feasible, intensity mapping experiments often outperform galaxy redshift surveys when measuring the mean [CII] intensity. For steep luminosity functions, intensity mapping appears to be the only means of measuring mean intensity and thus constraining the bulk of the luminosity function, as well as the optimal method of measuring the clustering power spectrum.

Although beyond the scope of this paper, our findings here reinforce the notion that the $z > 6$ Universe presents an ideal opportunity to learn about galaxy populations via intensity mapping. Strong evidence for steep ($\alpha \sim -2.0$) luminosity functions in the rest frame UV at $z \sim 7$ (Bouwens et al. 2014), as well as larger beam sizes for a given aperture at higher redshifts, combine to position intensity mapping more favorably compared to galaxy surveys in probing the nature and clustering of the reionizing population.

APPENDIX

To explore the effect of the luminosity function shape on the relative performances of intensity mapping and galaxy surveys in observing the [CII] power spectrum and mean intensity of [CII] emitters, we have introduced toy models to represent different $\Phi(L_{IR}, z) \equiv \frac{\mathrm{d}N}{\mathrm{d}L_{IR}\mathrm{d}V}$.

We parametrize our luminosity function as a Schechter function

$$\Phi(L_{IR}, z)\mathrm{d}L_{IR} = n_* \left(\frac{L_{IR}}{L_*}\right)^{\alpha} \exp\left(-\frac{L_{IR}}{L_*}\right) \mathrm{d}\left(\frac{L_{IR}}{L_*}\right) \tag{1}$$

where n_* is the normalization for number density, L_* is the characteristic luminosity at the knee, and α is the faint-end slope, as usual.

Power-law luminosity functions are notoriously ill-behaved if the lower limit of integration for either the luminosity functions or its moments is extended to zero. Rather than implement a break in the power law, we simply cut it off at some $L_{IR,min}$ and choose to fix in our analysis the total IR luminosity density from galaxies as predicted by B11, denoted as ρ_{IR}^{B11}, such that

$$\int d\left(\frac{L_{IR}}{L_*}\right) n_* L_* \left(\frac{L_{IR}}{L_*}\right)^{\alpha+1} \exp\left(-\frac{L_{IR}}{L_*}\right) \equiv \rho_{IR}^{\mathrm{B11}} \tag{2}$$

This is motivated by the observation that in many cases we do have constraints on the integrated light (from, for example, the cosmic infrared background or from the cosmic star formation rate density or the requirement of critical reionization), whereas we may not in general have detailed constraints on the distribution of light among galaxies, i.e., the shape of luminosity function.

The number density of sources, n, can, in turn, be computed from

$$n = \int d\left(\frac{L_{IR}}{L_*}\right) n_* \left(\frac{L_{IR}}{L_*}\right)^{\alpha} \exp\left(-\frac{L_{IR}}{L_*}\right) \tag{3}$$

Finally, equation 2 allows us to calculate the [CII] luminosity density for each IR-normalized toy model as

$$\rho_{[\mathrm{CII}]} = \int d\left(\frac{L_{IR}}{L_*}\right) n_* L_* \left(\frac{L_{IR}}{L_*}\right)^{\alpha} f_{[\mathrm{CII}]} L_{IR} \exp\left(-\frac{L_{IR}}{L_*}\right) \tag{4}$$

where $f_{[\mathrm{CII}]}$ is the fraction of IR luminosity emitted in [CII], or $\frac{L_{[\mathrm{CII}]}(L_{IR})}{L_{IR}}$, described by the Spinoglio relations. Because $L_{[\mathrm{CII}]}$ is slightly sublinear in L_{IR}, it follows that the toy models with steep faint-end slopes will produce more [CII] emission than their flatter counterparts.

REFERENCES

Béthermin, M., Dole, H., Lagache, G., Le Borgne, D., & Penin, A. 2011, A&A, 529, A4
Bouwens, R. J. et al. 2014, ArXiv e-prints
Brauher, J. R., Dale, D. A., & Helou, G. 2008, ApJS, 178, 280
Burgarella, D. et al. 2013, A&A, 554, A70
Carilli, C. L. 2011, ApJ, 730, L30
Casey, C. M., Narayanan, D., & Cooray, A. 2014, ArXiv e-prints
Chang, T.-C., Pen, U.-L., Bandura, K., & Peterson, J. B. 2010, ArXiv e-prints 1007.3709
Colbert, J. W. et al. 1999, ApJ, 511, 721
Cooray, A. et al. 2010, A&A, 518, L22
Dale, D. A., Helou, G., Brauher, J. R., Cutri, R. M., Malhotra, S., & Beichman, C. A. 2004, ApJ, 604, 565
de Putter, R., Holder, G. P., Chang, T.-C., & Dore, O. 2014, ArXiv e-prints
Díaz-Santos, T. et al. 2013, ApJ, 774, 68
Dole, H. et al. 2006, A&A, 451, 417
Ferkinhoff, C. et al. 2011, ApJ, 740, L29
Garnett, D. R., Edmunds, M. G., Henry, R. B. C., Pagel, B. E. J., & Skillman, E. D. 2004, AJ, 128, 2772
Glenn, J. et al. 2010, MNRAS, 409, 109
Gong, Y., Cooray, A., Silva, M., Santos, M. G., Bock, J., Bradford, C. M., & Zemcov, M. 2012, ApJ, 745, 49
Gong, Y., Cooray, A., Silva, M. B., Santos, M. G., & Lubin, P. 2011, ApJ, 728, L46
Graciá-Carpio, J. et al. 2011, ApJ, 728, L7
Hailey-Dunsheath, S., Nikola, T., Stacey, G. J., Oberst, T. E., Parshley, S. C., Benford, D. J., Staguhn, J. G., & Tucker, C. E. 2010, ArXiv e-prints 1003.2174
Hopkins, A. M. & Beacom, J. F. 2006, ApJ, 651, 142

Jullo, E. et al. 2012, ApJ, 750, 37
Kennicutt, Jr., R. C. 1998, ApJ, 498, 541
Lebouteiller, V. et al. 2012, A&A, 548, A91
Lester, D. F., Dinerstein, H. L., Werner, M. W., Watson, D. M., Genzel, R., & Storey, J. W. V. 1987, ApJ, 320, 573
Lidz, A., Furlanetto, S. R., Oh, S. P., Aguirre, J., Chang, T.-C., Doré, O., & Pritchard, J. R. 2011, ApJ, 741, 70
Luhman, M. L. et al. 1998, ApJ, 504, L11
Malhotra, S. et al. 1997, ApJ, 491, L27
—. 2001, ApJ, 561, 766
Morales, M. F. & Wyithe, J. S. B. 2010, ARA&A, 48, 127
Nagao, T., Maiolino, R., Marconi, A., & Matsuhara, H. 2011, A&A, 526, A149
Parsons, A. R. et al. 2013, ArXiv e-prints 1304.4991
Planck Collaboration et al. 2013, ArXiv e-prints
Rubin, R. H. 1985, ApJS, 57, 349
Sargsyan, L. et al. 2012, ApJ, 755, 171
Smith, R. E. et al. 2003, MNRAS, 341, 1311
Spinoglio, L., Dasyra, K. M., Franceschini, A., Gruppioni, C., Valiante, E., & Isaak, K. 2012, ApJ, 745, 171
Stacey, G. J., Hailey-Dunsheath, S., Ferkinhoff, C. an d Nikola, T., Parshley, S. C., Benford, D. J., Staguhn, J. G., & Fiolet, N. 2010, ApJ, 724, 957
Switzer, E. R. et al. 2013, MNRAS, 434, L46
Tingay, S. J. et al. 2013, Journal of Physics Conference Series, 440, 012033
Viero, M. P. et al. 2012, ArXiv e-prints
Visbal, E. & Loeb, A. 2010, J. Cosmology Astropart. Phys., 11, 16
Visbal, E., Trac, H., & Loeb, A. 2011, J. Cosmology Astropart. Phys., 8, 10